

## Measurement of the $\gamma\gamma^* \rightarrow \pi^0$ transition form factor

---

**M. Dubrovin\*** (On behalf of the BABAR Collaboration)<sup>†</sup>

*University of Cincinnati, USA*

*E-mail: dubrovin@slac.stanford.edu*

We study the reaction  $e^+e^- \rightarrow e^+e^-\pi^0$  in the single tag mode and measure the differential cross section  $d\sigma/dQ^2$  and the  $\gamma\gamma^* \rightarrow \pi^0$  transition form factor in the momentum transfer range from 4 to 40  $\text{GeV}^2$ . At  $Q^2 > 10 \text{ GeV}^2$  the measured form factor exceeds the asymptotic limit predicted by perturbative QCD. The analysis is based on  $442 \text{ fb}^{-1}$  of integrated luminosity collected at PEP-II with the BABAR detector at  $e^+e^-$  center-of-mass energies near 10.6 GeV.

*Light Cone 2010: Relativistic Hadronic and Particle Physics*  
*June 14-18, 2010*  
*Valencia, Spain*

---

\*Speaker.

<sup>†</sup>BABAR-PROC-10/031.

## 1. Introduction

In this conference presentation we discuss the process

$$e^+e^- \rightarrow e^+e^-\pi^0, \quad (1.1)$$

where the final state  $\pi^0$  is produced via two-photon mechanism [1], illustrated in Fig. 1. We measure [2] the differential cross section for this process in the single tag mode where one of the outgoing electrons<sup>1</sup> (tagged) is detected while the other electron (untagged) is scattered at a small angle and escape detection. The  $\pi^0$  is observed through its decay into two photons. The tagged electron emits a highly off-shell photon with the momentum transfer  $q^2 \equiv -Q^2 = (p - p')^2$ , where  $p$  and  $p'$  are the four momenta of the initial and final electrons. The momentum transfer of the untagged electron is near zero. The differential cross section for pseudoscalar meson production  $d\sigma(e^+e^- \rightarrow e^+e^-\pi^0)/dQ^2$  extracted from the experiment depends on only one form factor  $F(Q^2)$ , which describes the  $\gamma\gamma^* \rightarrow \pi^0$  transition. To relate the differential cross sections to the transition form factor we use the formula for  $e^+e^- \rightarrow e^+e^-\pi^0$  cross section in Eqs.(2.1) and (4.5) from Ref. [1].

At large momentum transfer,  $Q^2$ , perturbative QCD (pQCD) predicts that the transition form factor can be presented as a convolution of a calculable hard scattering amplitude for  $\gamma\gamma^* \rightarrow q\bar{q}$  with a non-perturbative pion distribution amplitude,  $\phi_\pi(x)$  [3]. The latter can be interpreted as the transition amplitude of the pion with momentum  $P$  into two quarks with momenta  $Px$  and  $P(1-x)$ . In lowest order pQCD the transition form factor is obtained from

$$Q^2 F(Q^2) = \frac{\sqrt{2}f_\pi}{3} \int_0^1 \frac{dx}{x} \phi_\pi(x) + O(\alpha_s) + O\left(\frac{\Lambda_{QCD}^2}{Q^2}\right), \quad (1.2)$$

where  $f_\pi = 0.131$  GeV is the pion decay constant. The pion distribution amplitude (DA) plays an important role in theoretical descriptions of many hard-scattering QCD processes. Since the evolution of  $\phi_\pi(x)$  with  $Q^2$  is predicted by pQCD, experimental data on the transition form factor can be used to determine its unknown dependence on  $x$  [4, 5, 6, 7, 8, 9, 10, 11].

The pion transition form factor was measured in the CELLO [12] and CLEO [13] experiments in the momentum transfer ranges of 0.7–2.2 GeV<sup>2</sup> and 1.6–8.0 GeV<sup>2</sup>, respectively. In this analysis we study the form factor in the  $Q^2$  range from 4 to 40 GeV<sup>2</sup>.

## 2. The BABAR detector and data samples

We analyze a data sample corresponding to an integrated luminosity of about 442 fb<sup>-1</sup> recorded with the BABAR detector [14] at the PEP-II asymmetric-energy storage rings. At PEP-II, 9-GeV electrons collide with 3.1-GeV positrons to yield a center-of-mass energy of 10.58 GeV (the  $\Upsilon(4S)$  resonance). Additional data ( $\sim 10\%$ ) recorded at 10.54 GeV are included in the present analysis.

Charged-particle tracking is provided by a five-layer silicon vertex tracker (SVT) and a 40-layer drift chamber (DCH), operating in a 1.5-T axial magnetic field. The transverse momentum resolution is 0.47% at 1 GeV/ $c$ . Energies of photons and electrons are measured with a CsI(Tl)

<sup>1</sup>Unless otherwise specified, we use the term “electron” for either an electron or a positron.

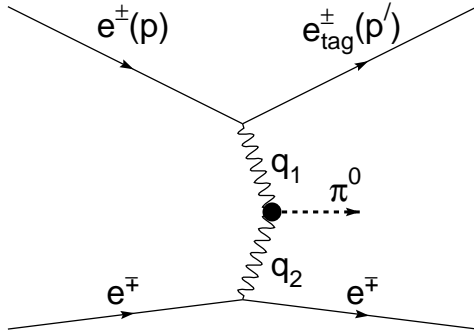


**Figure 1:** The Feynman diagram for the  $e^+e^- \rightarrow e^+e^-\pi^0$  two-photon production process.

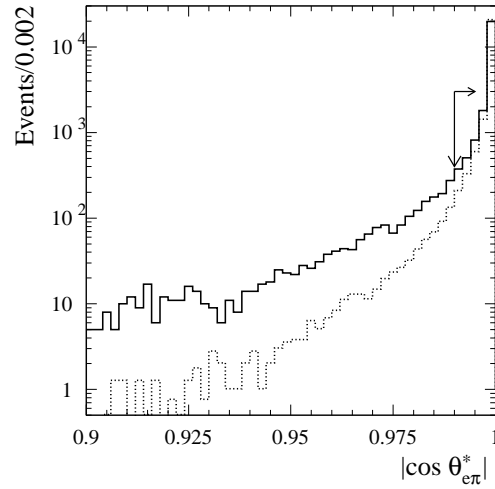


**Figure 2:** The distribution of the cosine of the polar angle of the  $e\pi^0$  system momentum in the c.m. frame for data (solid histogram) and simulated signal (dotted histogram). Events for which  $|\cos \theta_{e\pi^0}^*| > 0.99$  (indicated by the arrow) are retained.

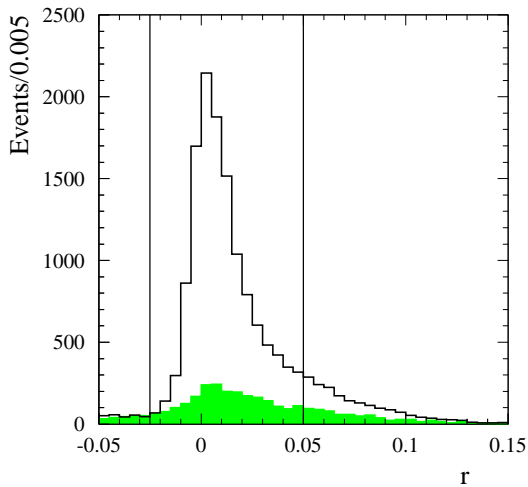


**Figure 3:** The  $r$  distribution for data events. The shaded histogram shows the background distribution, estimated from sidebands of the two-photon mass distribution. The vertical lines indicate the region ( $-0.025 < r < 0.050$ ) used to select candidate events.

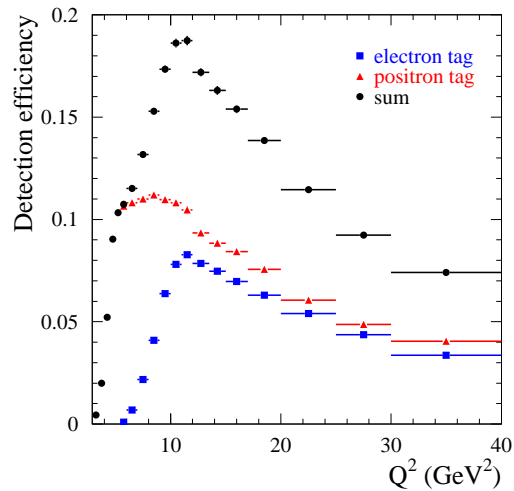


**Figure 4:** The detection efficiency as a function of  $Q^2$  for events with a tagged electron (squares), a tagged positron (triangles), and their sum (circles).

electromagnetic calorimeter (EMC) with a resolution of 3% at 1 GeV. Charged-particle identification is provided by specific ionization ( $dE/dx$ ) measurements in the SVT and DCH, and by an

internally reflecting ring-imaging Cherenkov detector (DIRC).

Signal and background  $e^+e^- \rightarrow e^+e^-\pi^0\pi^0$  processes are simulated with the Monte Carlo (MC) event generator GGRc. It uses the formula for the differential cross section from Ref. [1] for  $\pi^0$  production and the BGSM formalism [15] for the two-pion final state. Because the  $Q^2$  distribution is peaked near zero, the MC events are generated with a restriction on the momentum transfer of one of the electrons:  $Q^2 = -q_1^2 > 3 \text{ GeV}^2$ . This restriction corresponds to the limit of detector acceptance for the tagged electron. The second electron is required to have momentum transfer  $-q_2^2 < 0.6 \text{ GeV}^2$ . The experimental criterion providing this restriction for data events is discussed in Sec. 3. The pseudoscalar form factor is fixed to  $F(0)$  in MC simulation.

The GGRc event generator includes next-to-leading-order radiative corrections to the Born cross section calculated according to Ref. [16]. In particular, it generates extra soft photons emitted by the initial and final state electrons. The formula from Ref. [16] were modified to account for the hadron contribution to the vacuum polarization diagrams. The maximum energy of the extra photon emitted from the initial state is restricted by the requirement  $E_\gamma^* < 0.05\sqrt{s}$ , where  $\sqrt{s}$  is the  $e^+e^-$  center-of-mass (c.m.) energy. The generated events are subjected to detailed detector simulation based on GEANT4 [17], and are reconstructed with the software chain used for the experimental data. Variations in the detector and in the beam background conditions are taken into account. In particular, we simulate the beam-induced background, which may lead to appearance of extra photons and tracks in the event of interest, by overlaying the raw data from a random trigger event on each generated event. Background events from  $e^+e^- \rightarrow q\bar{q}$ , where  $q$  represents a  $u, d, s$  or  $c$  quark,  $e^+e^- \rightarrow \tau^+\tau^-$ , and  $e^+e^- \rightarrow B\bar{B}$  are simulated with the JETSET [18], KK2F [19], and EvtGen [20] event generators, respectively.

### 3. Event selection

At the trigger level the events for the process under study are selected by the *VirtualCompton* filter. This filter was originally designed to select so-called Virtual Compton Scattering (VCS) used for detector calibration. This process corresponds to  $e^+e^- \rightarrow e^+e^-\gamma$  reaction with kinematics requirement that one of the final electrons goes along beam axis, while the other electron and the photon are scattered at large angles. The filter requires that a candidate event contains a track with  $p^*/\sqrt{s} > 0.1$  and a cluster in the EMC with  $E^*/\sqrt{s} > 0.1$  which is approximately opposite in azimuth ( $|\delta\phi^* - \pi| < 0.1$  rad). Cluster and track polar angle acolinearity in the c.m. frame is required to be greater than 0.1 rad. Finally, the measured missing energy in c.m. frame, which should correspond to the undetected electron, is compared to a prediction based entirely on the directions of the detected particles and the assumption that the missing momentum is directed along the collision axis:  $|E_{meas}^* - E_{pred}^*|/\sqrt{s} > 0.05$ . For significant fraction of the  $e^+e^- \rightarrow e^+e^-\pi^0$  events the trigger cluster algorithm cannot separate the photons from  $\pi^0$  decay, and hence identify them as a single photon. Therefore the *VirtualCompton* filter has relatively large efficiency (about 50–80% depending on the  $\pi^0$  energy) for signal events.

In each event selected by the *VirtualCompton* filter we search for an electron and a  $\pi^0$  candidates. A charged track identified as an electron must originate from the interaction point and be in

---

<sup>2</sup>Throughout this paper the asterisk denotes quantities in the  $e^+e^-$  c.m. frame.

the polar angular range  $0.376 < \theta_e < 2.450$  rad in the laboratory frame. The latter requirement is needed to provide high efficiency of the trigger track-finding algorithm and for good electron identification. To recover the electron energy loss due to bremsstrahlung radiation, both internal and in the detector material before the DCH, we look for EMC showers close to electron direction and combine their energies with the measured energy of the electron track. The resulted laboratory energy of the electron candidate must be greater than 2 GeV. Two photon candidates with the energies greater than 50 MeV are combined to form a  $\pi^0$  candidate by requiring that their invariant mass be in the range 0.06–0.21 GeV/ $c^2$  and that their laboratory energy sum be greater than 1.5 GeV. Since a significant fraction of events contains beam-generated spurious track and photon candidates, extra tracks and extra photons are allowed in an event.

The main background process, VCS, has a cross section several thousand times greater than that for the process under study. The VCS photon together with a soft photon, for example from beam background, may give the invariant mass value close to the  $\pi^0$  mass. Such background events are effectively rejected by requirements on the photon helicity angle  $|\cos \theta_h| < 0.8$  and on the  $\pi^0$  c.m. polar angle  $|\cos \theta_\pi^*| < 0.8$ . The photon helicity angle is defined as the angle between the decay photon momentum in the  $\pi^0$  rest frame and the  $\pi^0$  direction in the laboratory frame.

The next step is to remove improperly reconstructed QED events. We remove events which involve noisy EMC channels, events with extra tracks close to the  $\pi^0$  candidate direction, and events with  $|\Delta\theta_{\gamma\gamma}| < 0.025$  rad, where  $\Delta\theta_{\gamma\gamma}$  is the difference between the laboratory polar angles of the photons from the  $\pi^0$  decay. The latter condition removes VCS events where the photon converted to a  $e^+e^-$  pair within DCH volume. It also removes about 20% of signal events, but significantly improves (by a factor of about 15) the signal-to-background ratio.

Two additional event kinematic requirements provide further background suppression and improve data to MC-simulation correspondence. Figure 2 shows the data and MC simulation distributions of the cosine polar angle of the  $e\pi^0$  system momentum in the c.m. frame. We require  $|\cos \theta_{e\pi}^*| > 0.99$ , that effectively limits the value of the momentum transfer to the untagged electron,  $q^2$ , and guarantees compliance with the condition  $-q_2^2 < 0.6$  GeV<sup>2</sup> used in MC simulation.

The emission of extra photons by the electrons involved leads to a difference between the measured and actual values of  $Q^2$ . In the case of initial state radiation (ISR) the  $Q_{meas}^2 = Q_{true}^2(1 + r_\gamma)$ , where  $r_\gamma = 2E_\gamma^*/\sqrt{s}$ . To restrict the energy of the ISR photon we use the parameter

$$r = \frac{\sqrt{s} - E_{e\pi}^* - p_{e\pi}^*}{\sqrt{s}}, \quad (3.1)$$

where  $E_{e\pi}^*$  and  $p_{e\pi}^*$  are the c.m. energy and the magnitude of the momentum of the detected  $e\pi^0$  system. In the ISR case this parameter coincides with  $r_\gamma$  defined above. The condition  $r < 0.075$  ensures compliance with the restriction  $r_\gamma < 0.1$  used in MC simulation. The  $r$  distribution for data is shown in Fig. 3, where the shaded histogram shows the background estimated from the fit of the two-photon mass distribution (Sec.4). We select events with  $-0.025 < r < 0.050$  for further analysis.

The background from  $e^+e^-$  annihilation into hadrons is strongly suppressed by the requirements of electron identification, on  $\cos \theta_{e\pi}^*$  and on  $r$ . An additional two-fold suppression of this background is provided by the condition that the  $z$ -component of the c.m. momentum of the  $e\pi^0$  system is negative (positive) for events with tagged positron (electron).

The  $Q^2$  dependence of the detection efficiency obtained from MC simulation is shown in Fig. 4. The detector acceptance limits the detection efficiency at small  $Q^2$ . To avoid possible systematics due to data-simulation difference near detector edges we measure the cross section and the form factor in the region  $Q^2 > 4 \text{ GeV}^2$ . The asymmetry of  $e^+e^-$  collision at PEP-II leads to different efficiencies for events with electron and positron tags. The  $Q^2$  range from 4 to 7  $\text{GeV}^2$  is measured only with the positron tag. The decrease of the detection efficiency in the region  $Q^2 > 10 \text{ GeV}^2$  is explained by the decrease of the  $\pi^0$  reconstruction efficiency due to growth of the average  $\pi^0$  energy with  $Q^2$ .

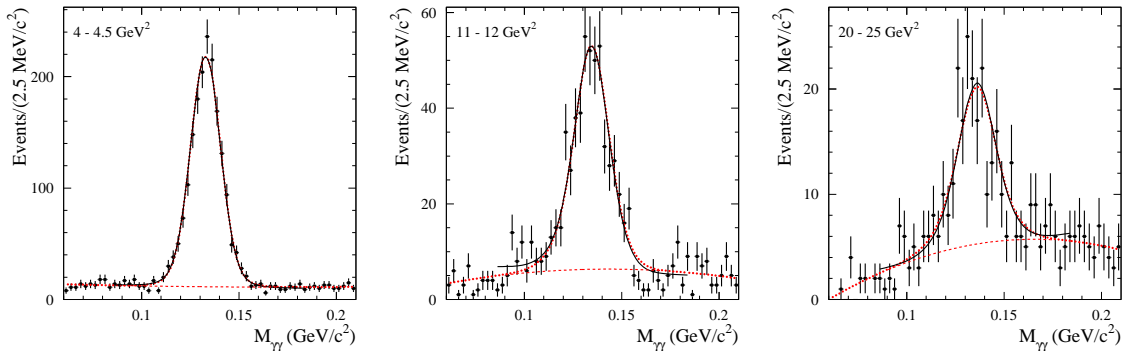


**Figure 5:** The two-photon invariant mass spectra for data events for three representative  $Q^2$  intervals. The solid (dotted) curve corresponds to the fit with linear (quadratic) background shape. The dashed curve represents the fitted quadratic background.

#### 4. Fitting two-photon mass spectrum

The two-photon mass spectrum for selected data events is shown in Fig. 5 for three  $Q^2$  intervals. For  $Q^2 > 40 \text{ GeV}^2$  we do not see evidence of a  $\pi^0$  signal over background. To determine the number of events containing a  $\pi^0$  we perform a binned likelihood fit to the spectrum with a sum of signal and background distributions. We describe the signal line shape by the sum of two functions from Ref. [21] with the same position of their maxima. The parameters of this signal function are fixed from the fit of the mass spectrum for simulated signal events weighted to yield the  $Q^2$  dependence observed in data. The background distribution is described either by a linear function in the mass range 0.085–0.185  $\text{GeV}/c^2$  or a second order polynomial in the mass range 0.06–0.21  $\text{GeV}/c^2$ . The data mass spectrum is fitted with 5 (6 for second order polynomial) free parameters: the number of signal events, the peak position, the width parameter,  $\sigma_1$ , of signal function, and 2 (3) parameters for background. The results of the fits are shown in Fig. 5.

The total number of signal events in the range of  $4 < Q^2 < 40 \text{ GeV}^2$  is about 14000. The difference in signal yield between the two background hypotheses is 170 events while the statistical error on the signal yield is 140 events. The difference between the peak positions in data and MC simulation is consistent with zero. The value of  $\sigma_1$  is 7.5  $\text{MeV}/c^2$  in data and 7.7  $\text{MeV}/c^2$  in simulation, which corresponds to the difference of about two standard deviations.

A similar fitting procedure is applied in each of the seventeen  $Q^2$  intervals indicated in Table I of Ref. [2]. The parameters of the  $\pi^0$  signal function are taken from the fit of the mass spectrum

for simulated events in the corresponding  $Q^2$  interval. For the fits to data, the value of the parameter  $\sigma_1$  is modified to take into account of the observed data-simulation difference in resolution:  $\sigma_1 \rightarrow \sqrt{\sigma_1^2 - (1.9 \text{ MeV})^2}$ . The free parameters in the data fits are the number of signal events and two or three parameters, depending upon the description of the background shape. The numbers of signal events obtained from the fits using linear background are listed in Table I of Ref. [2]. The difference between the fits in the two background hypotheses is used as an estimate of the systematic uncertainty associated with the unknown background shape.

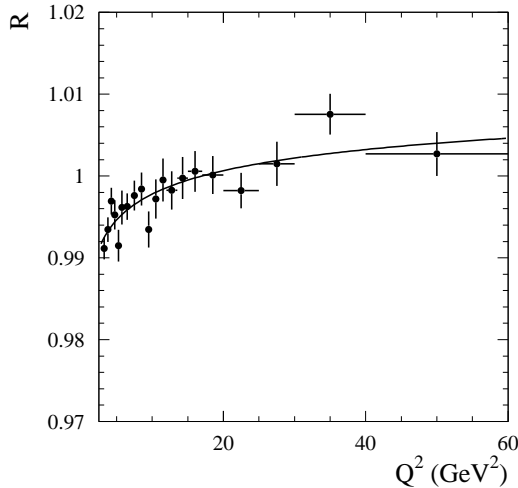


**Figure 6:** The  $Q^2$  dependence of the radiative correction factor.

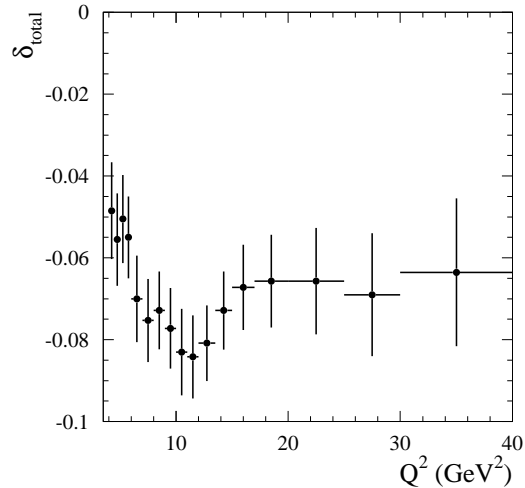


**Figure 7:** The  $Q^2$  dependence of the total efficiency correction.

## 5. Cross section and form factor

The differential cross section for  $e^+e^- \rightarrow e^+e^-\pi^0$  is calculated as

$$\frac{d\sigma}{dQ^2} = \frac{N_{corr}/\Delta Q^2}{\varepsilon RL}, \quad (5.1)$$

where  $N_{corr}$  is the number of signal events, corrected as discussed below,  $\Delta Q^2$  is the relevant  $Q^2$  interval,  $L$  is the total integrated luminosity  $442 \text{ fb}^{-1}$ ,  $\varepsilon$  is the detection efficiency obtained from simulation as a function of  $Q^2$ , Fig. 4, and  $R$  is a radiative correction factor.

The radiative correction factor accounts for distortion of the  $Q^2$  spectrum due to the emission of photons from the initial state particles and for vacuum polarization effects. It is determined from generator-based simulation. The  $Q^2$  spectrum is generated using only the Born amplitude for the  $e^+e^- \rightarrow e^+e^-\pi^0$  process, and then again using a model with radiative correction included. The  $Q^2$  dependence of the radiative correction factor, evaluated as the ratio of the second spectrum to the first, is shown in Fig 6. The accuracy of the radiative correction calculation is estimated to be 1% [16]. Note that the value of  $R$  depends on the requirement on the extra photon energy. The  $Q^2$  dependence obtained corresponds to the criterion  $r = 2E_\gamma^*/\sqrt{s} < 0.1$  imposed in the simulation.

The number of signal events,  $N_{corr}$ , is obtained from the mass spectrum yields after several corrections. First, we subtracted the background from the  $2\pi^0$  production  $e^+e^- \rightarrow e^+e^-\pi^0\pi^0$  process, peaking in the mass spectrum. The fraction of  $2\pi^0$  background events in the  $e\pi^0$  data sample changes from 13% for  $Q^2 < 10 \text{ GeV}^2$  to 6-7% for  $Q^2 > 10 \text{ GeV}^2$ . We do not see clear contribution from other two-photon processes, and estimate that their contribution do not exceed 5% of the  $2\pi^0$  background and thus are negligible. Then, we study the difference between data and MC-simulation for several well known processes and find the efficiency correction, defined as  $\delta = \varepsilon_{data}/\varepsilon_{MC} - 1$ . This correction accounts for effects of  $\pi^0$  identification efficiency, electron identification efficiency, trigger efficiency, kinematic requirements on  $r$  and  $\cos\theta_{e\pi}^*$ , and the effect of the beam-induced background. Total efficiency correction as a function of  $Q^2$  is shown in Fig. 7 and does not exceed 10%. Finally,  $N_{corr}$  also accounts the effect of finite  $Q^2$  resolution, by unfolding the migration matrix for statistics between adjacent bins. This effect changes the shape of the  $Q^2$  distribution insignificantly, but increases the errors (by about 20%) and their correlations.

The values of the differential cross section with statistical and systematic errors are listed in Table III of Ref. [2] and are shown in Fig. 8 together with CLEO data [13] for  $Q^2 > 4 \text{ GeV}^2$ . The  $Q^2$  independent systematic error is equal to 3% and includes the systematic uncertainties in the efficiency correction (2.5%), in the radiative correction factor (1%), and an error of total integrated luminosity (1%).

Since the requirement on  $\cos\theta_{e\pi}^*$  limits the momentum transfer of the untagged electron, we measure the cross section for the restricted  $q^2$  range  $|q^2| < a_{max}$ . The value of  $a_{max}$  is determined from the  $q^2$  dependence of the detection efficiency ( $\varepsilon(a_{max}) = 50\%$ ) and equal to  $0.18 \text{ GeV}^2$ .

To extract the transition form factor we compare the measured and the calculated values of the cross section. The simulation uses the constant form factor  $F_{MC}$ . Therefore the measured form factor is determined as

$$F^2(Q^2) = \frac{(d\sigma/dQ^2)_{data}}{(d\sigma/dQ^2)_{MC}} F_{MC}^2. \quad (5.2)$$

The calculated cross section  $(d\sigma/dQ^2)_{MC}$  has a model error due to the unknown dependence on the momentum transfer to the untagged electron. We use a  $q_2^2$  independent form factor, which corresponds to the QCD-inspired model  $F(q_1^2, q_2^2) \propto 1/q_1^2$  [24]. Using the vector dominance model with the form factor  $F(q_2^2) \propto 1/(1 - q_2^2/m_\rho^2)$ , where  $m_\rho$  is  $\rho$  meson mass, leads to a decrease of the cross section by 3.5%. This difference is considered to be an estimate of the model uncertainty due to the unknown  $q_2^2$  dependence. Note, that this estimate strongly depends on the limit on  $q_2^2$ . The value of 3.5% is obtained with  $|q_2^2| < 0.18 \text{ GeV}^2$ . For a less stringent  $q^2$  constraint, for example  $|q_2^2| < 0.6 \text{ GeV}^2$ , the difference between the calculated cross sections reaches 7.5%.

The values of the form factor obtained, represented in the form  $\overline{Q^2}|F(\overline{Q^2})|$ , are listed in Table III of Ref. [2] and shown in Fig. 9. For the form factor we quote the combined error, for which the statistical and  $Q^2$ -dependent systematic uncertainties are added in quadrature. The  $Q^2$ -independent systematic error is 2.3% and includes the uncertainty of the measured differential cross section and the model-dependent uncertainty due to the unknown  $q_2^2$  dependence.

## 6. Summary

We have studied the  $e^+e^- \rightarrow e^+e^-\pi^0$  reaction in the single tag mode and measured the differ-

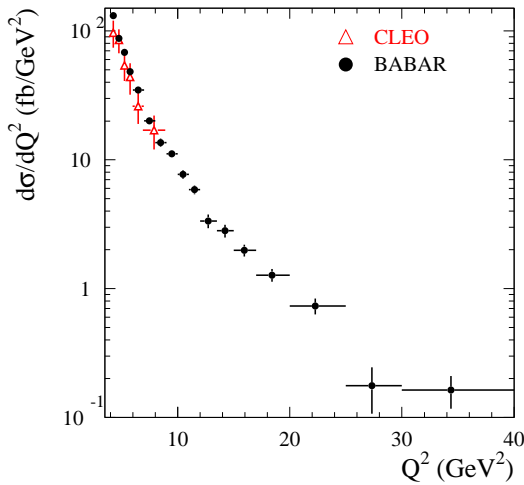


**Figure 8:** The  $e^+e^- \rightarrow e^+e^-\pi^0$  differential cross section obtained in this experiment compared to that from CLEO measurement [13].

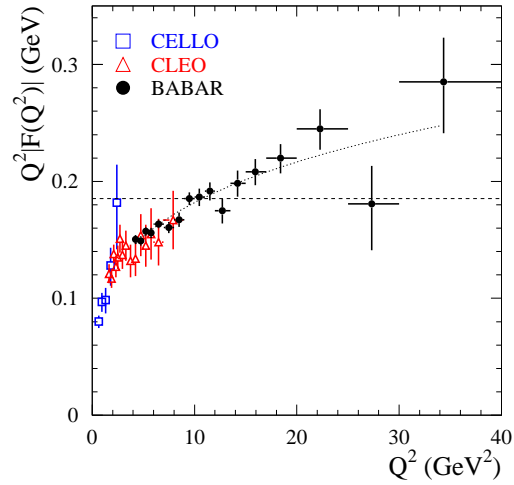


**Figure 9:** The  $\gamma\gamma^* \rightarrow \pi^0$  transition form factor multiplied by  $Q^2$ . The dashed line indicates the asymptotic limit for the form factor. The dotted curve shows the interpolation.

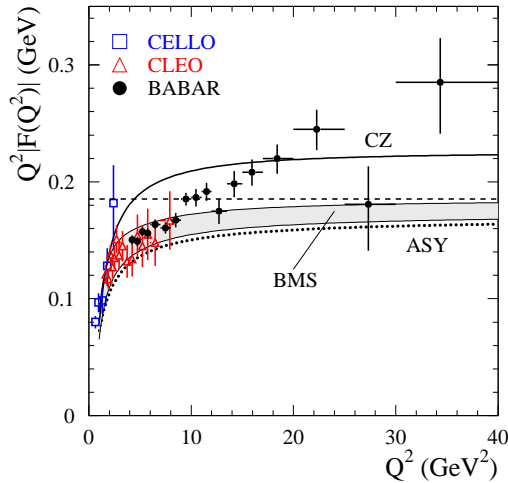


**Figure 10:** The  $\gamma\gamma^* \rightarrow \pi^0$  transition form factor multiplied by  $Q^2$ . The dashed line indicates the asymptotic limit for the form factor. The solid and dotted curves show the predictions for the form factor [9] for the CZ [27] and asymptotic (ASY) [28] models for the pion distribution amplitude, respectively. The shaded band represents the prediction for the BMS [29] pion distribution amplitude model.

ential cross sections ( $d\sigma/dQ^2$ ) and the  $\gamma\gamma^* \rightarrow \pi^0$  transition form factor  $F(Q^2)$  for the momentum transfer range from 4 to 40  $\text{GeV}^2$ . For the latter, the comparison of our results with the previous measurements [12, 13] is shown in Fig. 9. In the  $Q^2$  range from 4 to 9  $\text{GeV}^2$  our results are in a reasonable agreement with the measurements by the CLEO collaboration [13], but have significantly better accuracy. We also significantly extend the  $Q^2$  region over which the form factor is

measurement.

To effectively describe the  $Q^2$  dependence of the form factor in the range 4–40 GeV<sup>2</sup>, we fit the function

$$Q^2 |F(Q^2)| = A \left( \frac{Q^2}{10 \text{ GeV}^2} \right)^\beta \quad (6.1)$$

to our data. The values obtained for the parameters are  $A = 0.182 \pm 0.002 \text{ GeV}$  and  $\beta = 0.24 \pm 0.02$ . The fit result is shown in Fig. 9 by the dotted curve. The effective  $Q^2$  dependence of the form factor ( $\propto 1/Q^{3/2}$ ) differs significantly from the leading order pQCD prediction ( $\propto 1/Q^2$ ) (see Eq.1.2), demonstrating the importance of higher-order pQCD and power corrections in the  $Q^2$  region under study.

The horizontal dashed line in Fig. 9 indicates the asymptotic limit  $Q^2 F(Q^2) = \sqrt{2} f_\pi \approx 0.185 \text{ GeV}$  for  $Q^2 \rightarrow \infty$ , predicted by pQCD [3]. The measured form factor exceeds the limit for  $Q^2 > 10 \text{ GeV}^2$ . This contradicts most models for the pion distribution amplitude (see, e.g., Ref. [25] and reference therein), which give form factors approaching the asymptotic limit from below.

The comparison of the form factor data to the predictions of some theoretical models is shown in Fig. 10. The calculation of Ref. [9] was performed by A.P. Bakulev, S.V. Mikhailov and N.G. Stefanis using the light-cone sum rules method [26, 5] at the next-to-leading order (NLO) of pQCD; the power correction due to the twist-4 contribution [26] was also taken into account. Their results are shown for the Chernyak-Zhitnitsky DA (CZ) [27], the asymptotic DA (ASY) [28], and the DA derived from the QCD sum rules with non-local condensates (BMS) [29].

For all three DAs the  $Q^2$  dependence is almost flat for  $Q^2 \gtrsim 10 \text{ GeV}^2$ , whereas the data show significant growth of the form factor between 8 and 20 GeV<sup>2</sup>. This indicates that the NLO pQCD approximation with twist-4 power correction, which has been widely used for the description of the form-factor measurements by the CLEO collaboration [13], is inadequate for  $Q^2$  less than  $\approx 15 \text{ GeV}^2$ .

In the  $Q^2$  range from 20 to 40 GeV<sup>2</sup>, uncertainty due to higher order pQCD and power corrections are expected to be relatively small. Here, our data lie above the asymptotic limit, as does the prediction of the CZ model.

## Acknowledgments

I would like to thank organizers and participants of the Light Cone 2010 conference for excellent opportunity to present and discuss experimental and theoretical aspects of the  $\pi^0$  form factor measurement. I also thank my colleagues from BABAR and PEP-II, who have made this measurement.

## References

- [1] S. J. Brodsky, T. Kinoshita and H. Terazawa, Phys. Rev. D **4**, 1532 (1971).
- [2] B. Aubert *et al.* [BABAR Collaboration], Phys. Rev. D **80**, 052002 (2009).
- [3] G. P. Lepage and S. J. Brodsky, Phys. Rev. D **22**, 2157 (1980).
- [4] P. Kroll and M. Raulfs, Phys. Lett. B **387**, 848 (1996) [arXiv:hep-ph/9605264].

- [5] A. Schmedding and O. I. Yakovlev, Phys. Rev. D **62**, 116002 (2000) [arXiv:hep-ph/9905392].
- [6] N. G. Stefanis, W. Schroers and H. C. Kim, Eur. Phys. J. C **18**, 137 (2000) [arXiv:hep-ph/0005218].
- [7] E. Ruiz Arriola and W. Broniowski, Phys. Rev. D **66**, 094016 (2002) [arXiv:hep-ph/0207266].
- [8] A. P. Bakulev and S. V. Mikhailov, Phys. Rev. D **65**, 114511 (2002) [arXiv:hep-ph/0203046].
- [9] A. P. Bakulev, S. V. Mikhailov and N. G. Stefanis, Phys. Rev. D **67**, 074012 (2003) [arXiv:hep-ph/0212250], Phys. Lett. B **578**, 91 (2004) [arXiv:hep-ph/0303039].
- [10] S. S. Agaev, Phys. Rev. D **72**, 114010 (2005) [Erratum-ibid. D **73**, 059902 (2006)] [arXiv:hep-ph/0511192].
- [11] F. Feng, J. P. Ma and Q. Wang, JHEP **0706**, 039 (2007) [arXiv:0704.3782 [hep-ph]].
- [12] H. J. Behrend *et al.* [CELLO Collaboration], Z. Phys. C **49**, 401 (1991).
- [13] J. Gronberg *et al.* [CLEO Collaboration], Phys. Rev. D **57**, 33 (1998) [arXiv:hep-ex/9707031].
- [14] B. Aubert *et al.* [BABAR Collaboration], Nucl. Instr. and Meth. A **479**, 1 (2002).
- [15] V. M. Budnev, I. F. Ginzburg, G. V. Meledin and V. G. Serbo, Phys. Rept. **15**, 181 (1974).
- [16] S. Ong and P. Kessler, Phys. Rev. D **38**, 2280 (1988).
- [17] S. Agostinelli *et al.* [GEANT4 Collaboration], Nucl. Instr. and Meth. A **506**, 250 (2003).
- [18] T. Sjostrand, Comput. Phys. Commun. **82**, 74 (1994).
- [19] S. Jadach, B. F. L. Ward and Z. Was, Comput. Phys. Commun. **130**, 260 (2000) [arXiv:hep-ph/9912214].
- [20] D. J. Lange, Nucl. Instrum. Meth. A **462** (2001) 152.
- [21] A. D. Bukin, Preprint INP-2007-035, Novosibirsk, 2007.
- [22] H. Marsiske *et al.* [Crystal Ball Collaboration], Phys. Rev. D **41**, 3324 (1990); S. Uehara *et al.* [Belle Collaboration], arXiv:0805.3387 [hep-ex].
- [23] B. Aubert *et al.* [BABAR Collaboration], Phys. Rev. D **70**, 072004 (2004) [arXiv:hep-ex/0408078].
- [24] G. Kopp, T.F. Walsh, and P.M. Zerwas, Nucl. Phys. B **70**, 461 (1974).
- [25] N. G. Stefanis, arXiv:0805.3117 [hep-ph]
- [26] A. Khodjamirian, Eur. Phys. J. C **6**, 477 (1999) [arXiv:hep-ph/9712451].
- [27] V. L. Chernyak and A. R. Zhitnitsky, Nucl. Phys. B **201**, 492 (1982) [Erratum-ibid. B **214**, 547 (1983)].
- [28] G. P. Lepage and S. J. Brodsky, Phys. Lett. B **87**, 359 (1979).
- [29] A. P. Bakulev, S. V. Mikhailov and N. G. Stefanis, Phys. Lett. B **508**, 279 (2001).